Experimental and numerical analysis of drop-weight low-velocity impact tests on hybrid titanium composite laminates

Johannes Reiner[1,2], Juan Pablo Torres[3], Martin Veidt[1,2] and Michael Heitzmann[1,2]

Abstract

An experimental and numerical study on low-velocity impact responses on [Ti/0/90]$_s$ hybrid titanium composite laminates (HTCLs) is presented. Different energy levels from 10 to 40 J are investigated using a drop-weight instrument and post-impact inspection. An explicit finite element implementation provides a detailed analysis of impact response in composite and titanium layers, respectively. It accounts for interfacial debonding, progressive failure in composite plies and elastic–plastic deformation in titanium. The main failure modes are experimentally and numerically found to be debonding between titanium and composite, matrix cracking and interlaminar delamination. The principal energy-absorbing mechanism is plastic dissipation of the two titanium sheets. The low cost numerical model is able to effectively predict the overall impact response and major failure modes with good accuracy.

Keywords

Impact behaviour, finite element analysis (FEA), damage mechanics, fibre metal laminates

Introduction

Fibre metal laminates (FMLs) are increasingly finding use in a wide range of aerospace applications. Alternating metallic and composite layers improve fatigue, corrosion and fire and impact resistance[1] compared with monolithic structures. Due to their enhanced strength-to-weight ratios, FMLs are a promising feature to reduce fuel consumption in aircraft. The most well-known FML is glass laminate aluminium reinforced epoxy (GLARE) which is made from 2024 T3 aluminium alloy and S2-glass/epoxy sheets.[2] It is currently used for upper fuselage parts in Airbus A380 aircraft.[3] Another type of FML consists of titanium alloy sheets and carbon-fibre-reinforced composite. Hybrid titanium composite laminates (HTCLs) or titanium graphite (TiGr) can be found, for instance, in parts of the wings in Boeing's Dreamliner.[4] Future aerospace applications may approach high temperatures where the use of aluminium as a primary structure is not suitable, due to its insufficient creep resistance.[5] However, HTCLs are associated with engineering challenges such as increased corrosion potential owing to the addition of graphite[6] or processing damage caused by machining.[7] Other limitations, such as thermal expansion compatibility[8] or interfacial bonding,[9] are present but these are less significant compared with FMLs containing aluminium.

Low-velocity impact (LVI) response caused by bird-strike, tool drop or runway debris is of general concern to ensure long and safe service life with minimum maintenance.[10] LVI events in composite structures can cause barely visible impact damage (BVID) which is difficult to inspect and which can lead to catastrophic failure. Under these loading conditions, outer ductile metal layers in FMLs absorb most of the energy as plastic work.[1] Therefore, FMLs show superior impact

[1]School of Mechanical and Mining Engineering, The University of Queensland, Australia
[2]Centre of Advanced Materials Processing and Manufacturing (AMPAM), The University of Queensland, Australia
[3]Institute of Materials Science and Technology (INTEMA), Universidad Nacional de Mar del Plata-CONICET, Argentina

Corresponding author:
Martin Veidt, School of Mechanical and Mining Engineering, The University of Queensland, Brisbane, QLD 4072, Australia.
Email: m.veidt@uq.edu.au

performance to pure composite laminates.[11] Numerous experimental studies investigate impact responses of GLARE.[10,12,1] For instance, Liu and Liaw[10] compare different stacking sequences of aluminium and composite layers and identifies damage events such as delamination, matrix cracking and fibre breakage. Bernhardt et al.[13] compare HTCL samples with thin titanium sheets (0.13 mm thickness) to traditional composites. HTCLs show better impact resistance with a smaller damage zone. Cortes and Cantwell[14] considers different stacking sequences containing an additional thin titanium β alloy sheet (0.14 mm thickness) in the middle of the laminate for low and high velocity impact tests. Experimental results compare woven and cross-ply laminates. HTCLs with cross-ply cores show better impact properties in LVI with energy levels from 2 up to 10 J.

Laminates are typically modelled at the mesoscale level. With an increase of computational power, the complexity of LVIs can be reproduced more and more accurately by taking into account all failure modes and their interaction. Interlaminar damage is mainly modelled by means of cohesive elements. González et al.[15] discuss different modelling strategies using cohesive elements in regular and non-regular meshes or using surface-based cohesive interactions. By using non-zero thickness cohesive elements in a user-written material subroutine VUMAT, simulated LVI responses agree well with experimental findings in $[45_4/0_4/-45_4/90_4]_s$ and $[45_2/0_2/-45_2/90_2]_s$ composite laminates, respectively. Perillo et al.[16] investigate thick glass fibre composites numerically. Interfaces are represented by the cohesive damage model of Camanho et al.[17] which is available in the commercial software Abaqus. Furthermore, Puck and Schürmann's failure criterion for matrix cracking[18] and Hashin and Rotem's theory for fibre failure[19] are implemented in a material subroutine. The model predicts impact response well for energy levels ranging from 22.70 to 68.25 J. However, recent LVI simulations require a huge computational effort. Parallelisation in cluster computation is typically used. Models run for up to 15 days on 24 CPUs[15] or, more recently, for 48 hours on 32 CPUs.[16]

Compared with LVI simulations for composite laminates, HTCL simulations are less frequent in literature. Nakatani et al.[20] investigates $[Ti/0_3/90_3]_s$ laminates experimentally and numerically. Simulations in Abaqus at low energy levels at around 5 J predict the impact response well.

In this paper, effective modelling tools and techniques for general applications are developed. It contributes, in particular, to the scientific understanding of LVI phenomena by relating experimentally observed and simulated damage evolution with physical mechanisms. To the best of the authors' knowledge, computationally challenging high-energy impact simulations on HTCLs cannot be found in the literature. Models were run on a conventional computer for no longer than one day.

After material specifications and presentation of drop-weight test results, simulations are compared to experimental findings. Energy dissipation events due to plastic deformation and composite failure are numerically quantified and studied in detail. Their evolution and interaction explain the impact response, as well as material failure behaviour. Recommendations to further improve the numerical modelling conclude this paper.

Material data and sample preparation

HTCLs in this study are made from 0.5 mm thick Grade 2 titanium sheet and unidirectional Hexcel G947/M18 carbon-fibre-reinforced polymer (CFRP) plies of 0.165 mm thickness.

In order to characterise the mechanical properties of Grade 2 titanium accurately, standard tensile tests were performed in conjunction with two-dimensional digital image correlation (DIC).[21] Dogbone titanium samples were tested using an Instron 5584 mechanical testing frame fitted with hydraulic clamping cross-heads and 100 kN load cell. A constant displacement rate of 1 mm/min was applied according to ASTM E8 'Standard Test Methods for Tension Testing of Metallic Materials'. DIC allows for measuring local displacement or strain fields. Figure 1(a) shows a dogbone sample superimposed with the strain field measured by DIC. Strain accumulates in a localised area within the gauge length. All material properties were determined by analysing material data in this area. The true stress–strain graph is shown in Figure 1(b). Table 1 summarises the characteristic properties. In addition, it includes literature data on interface properties of Ti-15V-3Cr-3Sn-3Al β titanium alloy and M40-J/CYCOM 077-2 CFRP.[22]

Table 2 shows elastic properties and strengths of G947/M18 CFRP as well as fracture properties of a similar composition. Data is taken from the literature and material data sheets. The $[Ti/0/90]_s$ samples of dimensions $300 \times 300 \text{ mm}^2$ were manufactured according to Kennedy et al.'s guidelines.[23] To ensure strong interlaminar bonding between metal and prepreg layers, the titanium surface was treated as follows. First, sandpaper was used to increase the macro-roughness on the titanium. Then impurities on the surface were removed using MEK (methyl ethyl ketone). Finally, each titanium sheet was anodised in a highly concentrated 5 M NaOH solution for 30 minutes at 10 V. The stacked hybrid laminates were vacuum
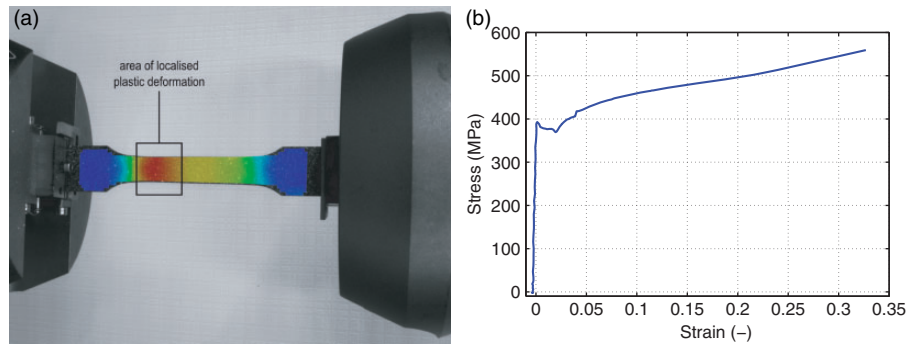
Figure 1: Experimental setup and result of Grade 2 titanium characterisation. (a) Tensile sample superimposed with DIC strain pattern and (b) True stress versus true strain.

Table 1: Grade 2 titanium properties.

Density	$\rho = 4.5 \times 10^{-6}$ kg/mm^3
Elastic properties	$E = 97.7$ GPa, $\nu = 0.37$
Yield strength	$\sigma_y = 349.02$ MPa
Interface Ti/comp[22]	$G_{Ic} = 179$ J/m^2 $G_{IIc} = 363$ J/m^2
Ply thickness	$t^{Ti} = 0.5$ mm

bagged and then cured according to Hexcel's cuing profile for G947/M18.

Drop-weight impact test

LVI tests are conducted using an in-house drop-weight test frame with rebound brake system to avoid multiple strikes. Two guide rails channel a falling weight of 3.0223 kg. The test set-up is shown in Figure 2. Attached to the falling weight, a hemispherical steel head (Dytran 1050V6) with a diameter of 25.4 mm is connected to a Tektronix TDS 420A oscilloscope through a dynamic load cell to measure impact force–time history. Different energy levels are achieved by varying height H_0, whereas the impactor mass is kept constant. Impact velocity is recorded by two-gate laser measurements just before impact. Test samples are fixed on a wooden frame support by eight clamps, as shown in Figure 2.

Impact energy is varied in 10 J increments up to 40 J. Figure 3 compares force–time histories for different energy levels. Short drops or non-smooth parts in the force response indicate damage events such as debonding, delamination, fibre breakage or matrix failure, and boundary effects. The force response is characterised by a bilinear increase up to the first significant drop ① at around 3 ms. The second significant drop ② in Figure 3(a) coincides with the maximum force which corresponds to the time when the impactor reverses.

Therefore the third peak ③ can be interpreted as pure boundary effects in the unloading phase. The intensity of these three peaks increases with increasing impact energy. Physical mechanisms causing the first drop ① are less intuitive compared to the other two characteristic events ② and ③. This issue is addressed in the next section. A computational study on failure modes will identify and quantify damage events related to that first drop in force response as well as overall characteristic features of experimental measurements.

Total energy in Figure 3(b) is calculated by integrating force versus displacement data. After reaching maximum force, the energy drops to a constant value. This indicates that rebound occurs in all cases. The constant value at the end corresponds to total absorbed energy. The ratio of absorbed and initial impact energy is shown in Figure 3(c). The graph implies an increase in absorbed energy which indicates that more energy is dissipated. Considering HTCL samples, the dissipated energy is caused by plastic deformation in the titanium and interlaminar and intralaminar damage in the composite and titanium–composite interface.

Some of the tested HTCL samples were sectioned through the impact location to inspect failure modes. This was necessary because imaging by non-destructive ultrasonic pulse-echo C-Scan testing using an Olympus OmniScan MX2 flaw detector with a 5 MHz universal phased array probe was not successful due to the small thickness of the individual constituents and the overall samples. Figure 4 shows the cross section of a sample subjected to 40 J. A significant debonded area ① is visible between the bottom titanium sheet and the composite laminate. The length is approximately 20 mm. Moreover, all typical failure modes in impacted composite laminates such as delamination, matrix failure and fibre breakage can be observed. In the central part of the cross section, two oblique through-thickness matrix cracks in the two 90° layers ② exist and initiate interlaminar delamination ③. Additionally, fibres fail in the lower 0° layer ④. It can be concluded that bending

Table 2: G947/M18 carbon/epoxy unidirectional properties.

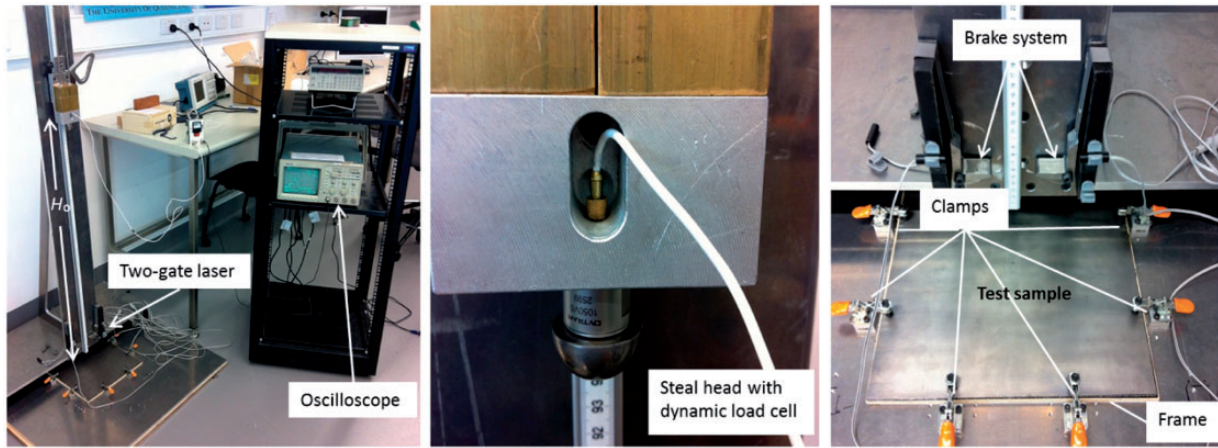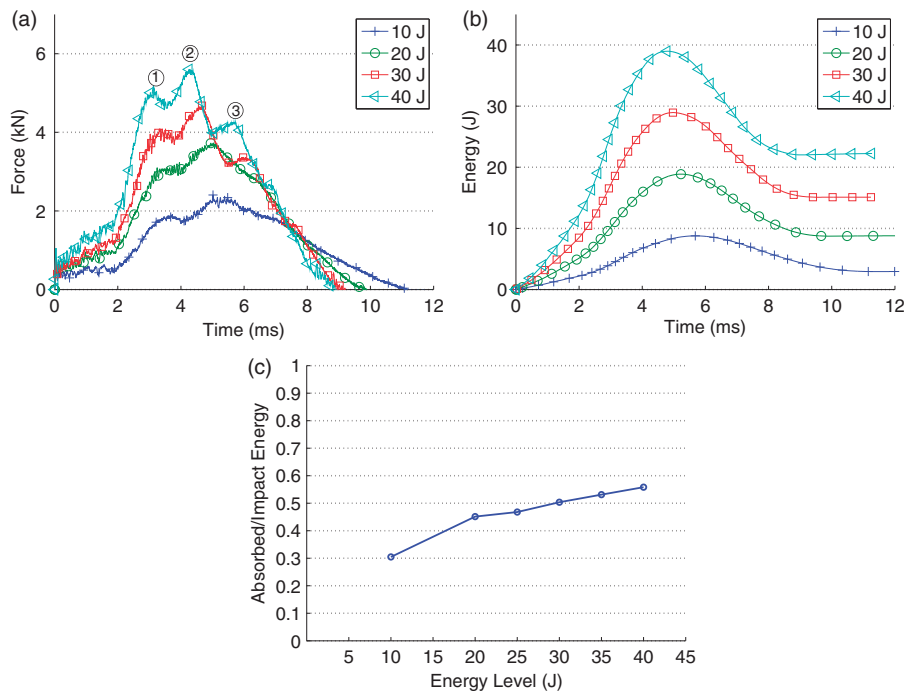| Density[36]	$\rho = 1.22 \times 10^{-6}$ kg/mm^3					
Elastic properties[37]	E_{11} (GPa)	$E_{22} = E_{33}$ (GPa)	$G_{12} = G_{13}$ (GPa)	G_{23} (GPa)	$\nu_{12} = \nu_{13}$	ν_{23}
	97.6	8.0	3.1	2.7	0.37	0.5
Strength[36]	X_T (MPa)	X_C (MPa)	Y_T (MPa)	Y_C (MPa)	S_L (MPa)	
	1750	1500	55	220	95	
Fracture properties[38]	G_{Ic} (J/m^2)	G_{IIc} (J/m^2)				
	250	500				
Ply thickness	$t_{CF} = 0.165$ mm					

Figure 2: Drop-weight test frame.

Figure 3: Comparison of tested HTCLs subjected to different energy levels. (a) Impact force versus time, (b) Absorbed energy versus time and (c) Ratio of absorbed/impact energy.
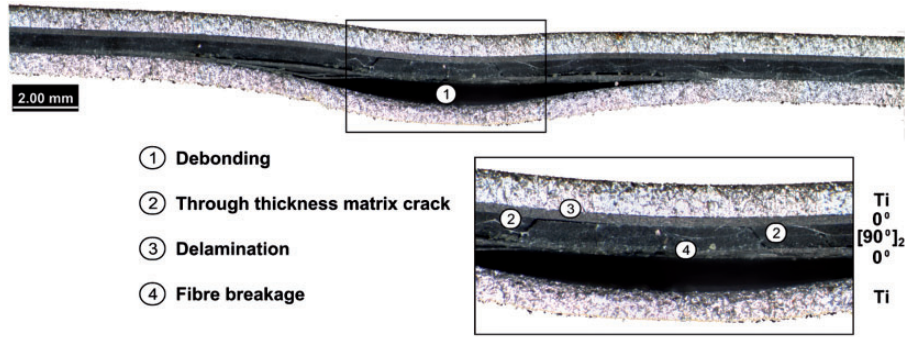
Figure 4: Optical inspection of HTCL sample subjected to 40 J.

in tension in the lower part of the sample causes more damage compared to compression in the upper part. These phenomena can also be found in other FMLs. GLARE 5-2/1 resembles the tested HTCL in terms of thickness and stacking. It is 1.562 mm thick and it consists of two aluminium layers and glass-reinforced epoxy prepreg with 0°/90°/90°/0° fibre orientation. Impacted to 12.7 J, Wu et al.[12] identify similar failure modes such as debonding around the point of impact and 45° inclined matrix cracks propagating into interlaminar delamination between the glass-fibre-reinforced composite plies.

Computational study

Constitutive model and failure criteria

Constitutive model. Titanium is modelled as isotropic linear elastic with associated plastic flow using a von Mises yield surface with isotropic hardening. The composite layers follow an orthotropic linear elastic behaviour with an associated damage initiation and evolution law. The modified lamina stiffness matrix due to damage is given by

$$\mathbb{C} = (1 - \boldsymbol{d})\mathbb{C}_0 \tag{1}$$

where $\mathbb{C}_0$ is the initial undamaged stiffness matrix and $\boldsymbol{d}$ is a diagonal matrix with scalar damage variables d_i, $i = 1, \ldots, 6$ ranging between 0 and 1. These variables describe the stiffness degradation in longitudinal (fibre) and in transverse (matrix) directions and in mixed-mode behaviour.

Damage activation and evolution. A damage activation function for a failure mode N is[24]

$$F_N = \phi_N - r_N \leq 0 \tag{2}$$

where ϕ_N, corresponding to a failure mode N, is a function of elastic and strength properties.

The internal variable r_N is related to the damage variable d_N. When material is undamaged, r_N equals

one. Once damage initiates, r_N increases monotonically such that[24]

$$r_N = \max\left(1, \max_{s=0,t}(\phi_N)\right) \tag{3}$$

In order to evaluate the damage variable d_N, a relationship between d_N and internal variable r_N is established. The variable d_N increases continuously with a simple exponential damage evolution such that[25]

$$d_N = 1 - \exp\left(\frac{1}{m}\left(1 - r_N^m\right)\right) \tag{4}$$

where m is a material constant for softening behaviour.

A more advanced model[24,26,15] uses critical energy release rates in conjunction with Bažant et al.'s crack band theory[27] in order to introduce mesh-independent damage evolution by exponential softening. In contrast to the simple approach in (4), the advanced model allows for complex loading such as tension–compression reversals.[24]

Failure criteria in composites. The World Wide Failure Exercise (WWFE-I and WWFE-II) investigated different failure theories about damage onset and evolution for typical failure modes in composites, for example delamination, matrix cracking or fibre breakage in two- and three-dimensional problems. Global failure criteria such as Tsai–Wu[28] do not distinguish between different failure modes. Phenomenological criteria such as Hashin[19] or Puck,[18] however, describe each failure mode individually. Continuum damage models, such as Matzenmiller[25] or Maimi,[24] include degradation functions to incorporate smooth damage evolution.

Here, four different failure criteria with and without degradation functions are assessed. These are: (1) Hashin, (2) Puck, (3) Tsai–Wu and (4) maximum stress criterion. A summary of the main equations for each model is presented in the Appendix. As seen in Figure 4, matrix cracking is the major failure mode
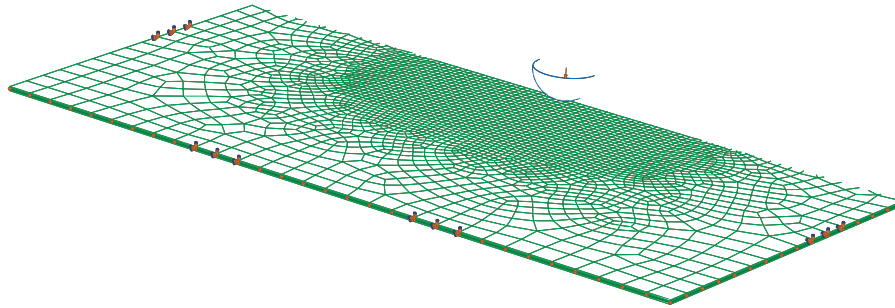
Figure 5: Boundary conditions and meshing applied to the HTCL sample and impactor in the finite element model. Only half of the model is shown. Simulations are performed on the full model.

inside the fibre-reinforced composite. This will be discussed in detail later.

Delamination/debonding. The cohesive zone method (CZM) is a well-established concept for modelling interlaminar delamination in composites or debonding between two different materials. With this technique, the bonded interface is modelled with cohesive elements that capture its initial loading, initiation of damage, and the propagation of damage leading to eventual failure. The behaviour of the interface prior to initiation of damage is described as linear elastic in terms of a penalty stiffness using a traction–separation-based model which relates applied cohesive tractions τ to a displacement jump Δ:[29] that is

$$\tau_i = (1 - d)\mathbb{D}_{ij}\Delta_j - d\mathbb{D}_{ij}\delta_{3j}\langle-\Delta_3\rangle \qquad (5)$$

with a diagonal stiffness tensor $\mathbb{D} = diag(K)$, where K is a scalar penalty stiffness. The second term prevents interpenetration in the through-thickness direction by contact. Here, δ_{ij} is the Kronecker delta and $\langle x \rangle = \frac{1}{2}(x + |x|)$ are Macaulay brackets. In order to describe the damage variable d, a specific law for damage onset and evolution needs to be defined. Information about implementation and applied criteria follows in next section.

Impact simulation

Finite element model. HTCL samples are implemented at mesoscale level in Abaqus/Explicit 6.11.[30] Figure 5 shows half of the finite element model including impactor, boundary conditions and mesh size. Around the central impact, a refined mesh of 2.5 mm × 2.5 mm is defined. Outside this region, the mesh is significantly coarser. In order to reproduce the experimental set-up realistically, nodes at the bottom edge are restrained to model the wooden frame base support. Fully restrained nodes are applied at the positions of the eight clamps

around the sample. Furthermore, motion of the rigid impactor is governed by a single reference point by specification of impact velocity and restriction to out-of-plane movement. Tangential friction between the steel impactor and the upper titanium plate is set to 0.33. Gravity is applied to the entire model.

All titanium and composite layers are modelled by means of C3D8R three-dimensional hexahedral continuum solid elements with eight nodes and reduced integration. Enhanced hourglass control and distortion control with length ratio 0.05 are activated. These features prevent instability problems and excessive distortion. Table 1 shows the elastic properties used for titanium and Figure 1 gives the tabular input used to govern plastic yielding with isotropic hardening. Composite plies are modelled as elastic orthotropic using engineering constants taken from Table 2. Criteria for matrix and fibre failure in Section 4.1 are implemented in a user-written FORTRAN material subroutine VUMAT. Furthermore, damage evolution in (4) is considered and user-defined elements are removed when the damage variable d_N reaches the value 0.95 using the element deletion option in Abaqus to further mitigate the effect of sudden element distortion. The residual stiffness in the corresponding active damage mode is then 5% of the initial stiffness component.

Cohesive elements determine the runtime analysis. According to the Courant condition, stable time increments decrease due to zero thickness elements.[15] In order to reduce computational cost, cohesive interface elements are only applied between the titanium and composite layers. Interfacial fracture properties in Tables 1 and 2, as well as damage inspection in Figure 4, show that decohesion in this interface is dominant as it is weaker compared with interlaminar failure in composites. Therefore, fracture properties in Table 2 are neglected. COH3D8 zero-thickness elements model the titanium–composite interface. To reduce distortion, cohesive elements are removed without any residual strength when the scalar damage variable d in (5)
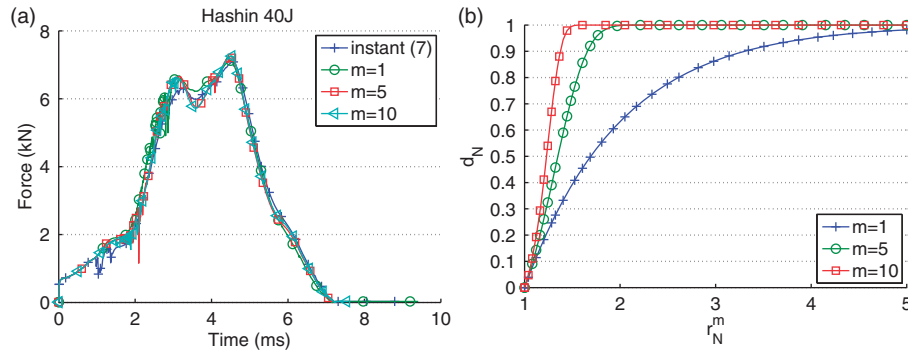
Figure 6: Numerical investigation of damage evolution in composite plies. (a) Comparison of damage evolution and b) Exponential damage evolution for varying m, according to equation (4).

reaches the value 0.9. An estimation for the initial penalty stiffness K of a symmetric laminate is given by[31]

$$K = \frac{\alpha E_3}{t} \qquad (6)$$

where t is the thickness of a sublaminate, E_3 is the through-thickness Young's modulus and $\alpha \gg 1$ is a material parameter. Turon et al.[31] state that for $\alpha \geq 50$, sufficient accuracy for most problems is achieved. With half the thickness of the HTCL sample ($t = 0.83$ mm and $\alpha = 50$), the initial stiffness of the interface is implemented as $K = 6.89 \times 10^5$ N/mm^3. Degradation in the cohesive element initiates from maximum cohesive traction $\tau_{\max} = 30$ MPa in (5). The choice of $\tau_{\max}$ has little effect on the decohesion behaviour[32] which is mostly governed by fracture energies G_{Ic} and G_{IIc} in Mode I and Mode II in Table 1, respectively. A linear softening with Benzeggagh–Kenane (BK)[33] mixed-mode behaviour and mixed-mode parameter η is chosen, as well as an appropriate viscosity coefficient, to stabilise the solution procedure. A typical value for the mixed-mode parameter in brittle epoxy resin such as M18 is $\eta = 1.75$.[17]

Results and discussion. The FE models run on a single core, single processor. The entire runtime analysis for each model is about 20 hours. In the following, further simplifications on damage evolution and choice of failure criteria in composites are discussed before relating numerical results to experimental findings.

m-parametric study. Hashin's failure criteria are used to investigate damage evolution according to equation (4) with maximum damage variable $d_N = 0.95$. A parametric study on the material parameter m in Figure 6(a) shows only a little influence on the overall impact response. Similar behaviour is predicted for $m = 1, 5, 10$. Evolution softens material degradation in composite plies. As can be seen in Figure 6(a), damage for small values of m is initiated later which is indicated by small variations in

the force response. Moreover, it gives slightly higher maximum force predictions as fewer elements are deleted from the mesh due to a softer damage evolution. The parametric study leads to a simple evolution where the damage variable d_N is instantaneously 0.95 at damage initiation

$$d_N = \begin{cases} 0 & \text{if } F_N < 0 \\ 0.95 & \text{if } F_N = 0 \end{cases} \qquad (7)$$

Figure 6(b) shows damage evolution for different values of m. High values approximate the implementation with instant damage in (7). It should be noted that this conclusion holds for maximum damage variable $d_N = 0.95$ in equation (4). This approximation can also be seen in the force response, where the model $m = 10$ almost matches the prediction of instant damage evolution.

Failure criteria. Figure 7 shows numerical results for impact energy ranging from 10 to 40 J. The simplified instant damage evolution in (7) is used. Figure 7(a) includes different failure criteria which are compared to experimental results. Hashin and Puck include criteria for fibre and matrix failure in tension and compression, respectively, whereas Tsai–Wu combines all failure modes to a global criterion. Each criterion is presented in detail in the Appendix. It can be observed that all implemented failure criteria give very similar responses. When impacting, $\sigma_{22} \gg \sigma_i$, $i = 33, 12, 13, 23$ and $\sigma_{11} \ll X_j$, $j = T, C$. Therefore, it becomes obvious that matrix failure is the dominant failure type. All tensile matrix failure criteria mentioned in Section 4.1 and the Appendix reduce to a simple maximum stress criterion without any significant alterations in the overall response prediction. In the case of HTCL with a relatively small proportion of composite and thick energy absorbing titanium sheets, it can be concluded that the choice of failure criteria is less significant than in pure composite laminates. Figure 7(b)–(d) shows Hashin's failure criteria applied to lower energy levels. Other failure criteria such as Puck or Tsai–Wu are not shown because of the similarity of the
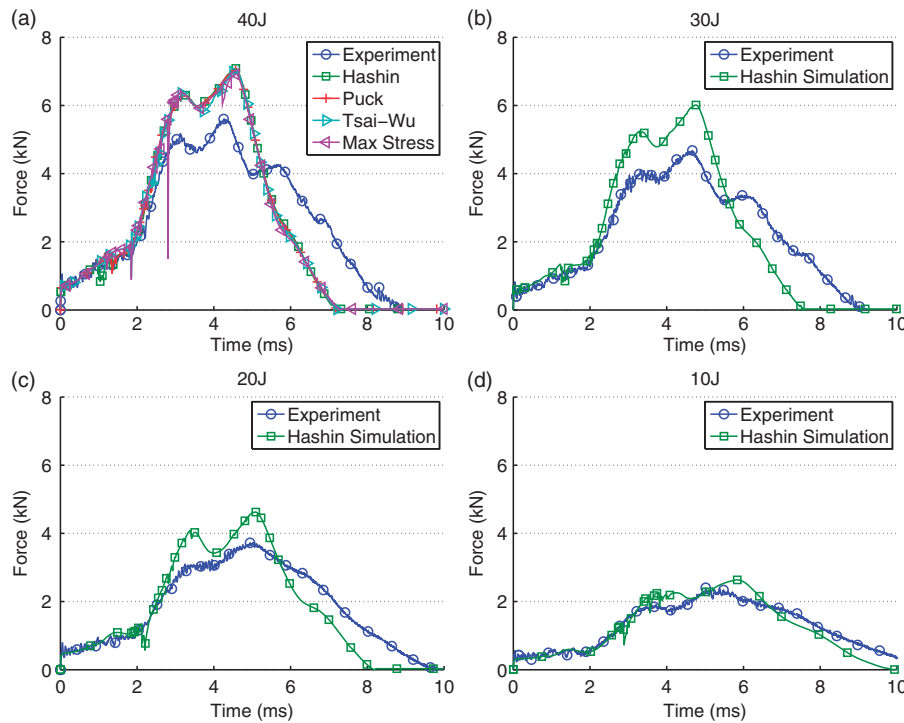
Figure 7: Numerical results for different failure criteria and energy levels with instant damage evolution in (7). (a) Comparison of failure criteria, (b) Force versus time: 30 J, (c) Force versus time: 20 J and (d) Force versus time: 10 J.

results. The simulations show good agreement. It can also be observed that accuracy increases with decreasing energy level. This is a common feature and it can also be found in computationally expensive LVI predictions for pure composite laminates.[15,16] Numerical simulations overestimate maximum force response by up to 20%. Sacrifices to model the impact response on a conventional computer in a reasonable time lead to such a difference. A finer mesh can capture debonding at the titanium–composite interface more precisely.[15] Zero-thickness cohesive elements for interlaminar delamination in composites can also improve accuracy of the model. Damage inspection in Figure 4 shows clearly visible delamination fronts between 0° and 90° layers. Furthermore, boundary conditions such as the wooden support frame and the clamps around the HTCL sample can be modelled as independent instances with contact properties.[16] All of these improvements significantly increase runtime analysis. Debonding in the titanium–composite interface was identified in Section 3 as a major failure mode. Therefore accurate interfacial fracture properties are required in order to model debonding precisely. Table 1 includes interface properties for Ti-15V-3Cr-3Sn-3Al β titanium alloy and M40-J/CYCOM 077-2 CFRP. Experimental tests are currently conducted to characterise interfacial behaviour of the Grade 2 titanium and G947/M18 CFRP used in this HTCL. However, this is not expected to significantly alter the results presented here.

Despite all simplifications, the bilinear increase up to the maximum force is represented well. Moreover, all models show good agreement with the significant drops ① and ② in Figure 3(a) at 3 and 5 ms, respectively. Compared with similar numerical investigations of pure composite samples using advanced computing techniques such as clustering, the presented model efficiently reduces runtime analysis on a conventional computer by up to 90%. Accurate identification and characterisation of major processes allow the use of finite element method results for a detailed failure analysis which can explain the experimental force–time response in Figure 3.

In the following, numerical results obtained by Hashin's failure criteria and the instant damage evolution in (7) are analysed.

Failure analysis. Using numerical simulation enables a detailed failure analysis by comparing different energy terms. Figure 8(a) compares the predicted and experimental total energy. The simulated total energy is given by a history output variable ALLIE in Abaqus. The graphs are normalised with respect to the experimental result of 40 J. Good agreement between experiments and simulations is achieved. In addition, Figure 8(b) shows dissipated energy due to plastic deformation in titanium and damage events in composites. The force response from Figure 7(a) is added in the background to relate dissipation events to it. History output
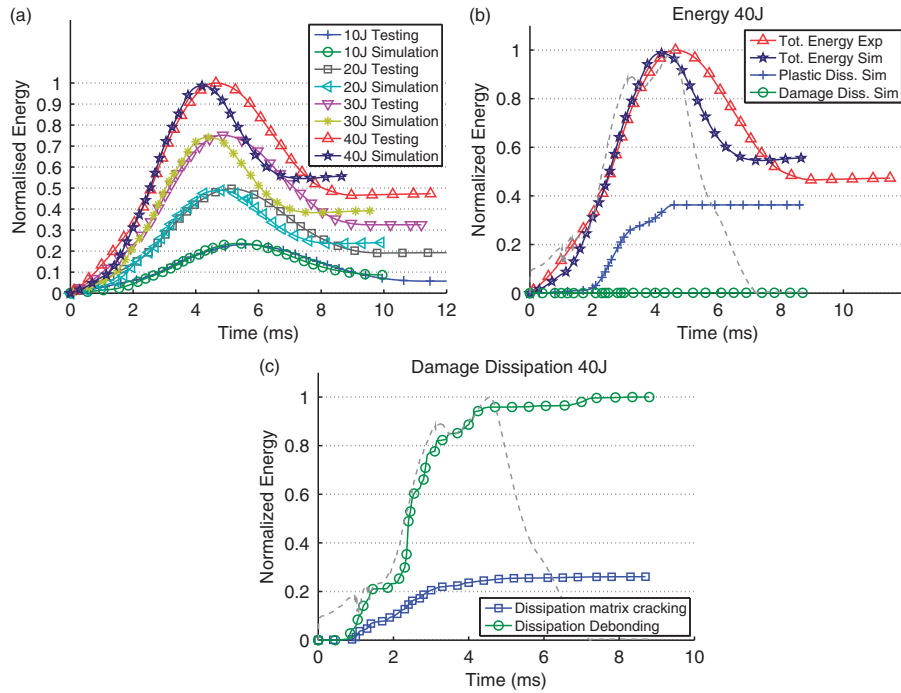
Figure 8: Energy analysis in impacted HTCL using Hashin's failure criteria and damage evolution in (7). (a) Total energy, (b) Energy mechanisms and (c) Damage dissipation.
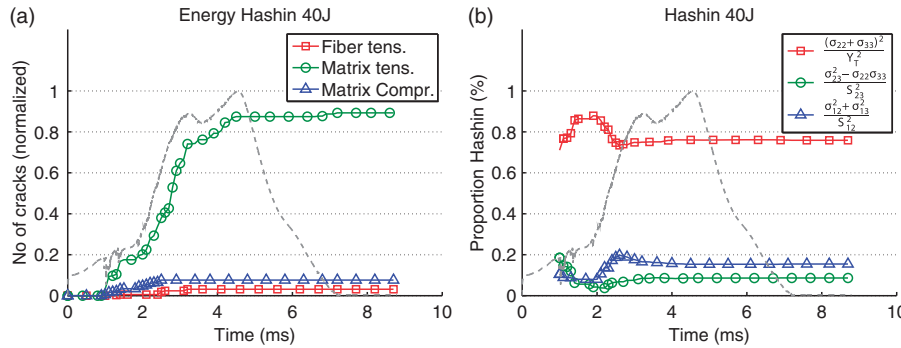

Figure 9: Failure analysis in composite plies and investigation of Hashin's matrix failure criterion. (a) Damage contribution and (b) Hashin matrix failure criterion.

ALLDMD in Abaqus represents debonding dissipation, whereas a solution-dependent state variable (SDV) inside the user-subroutine VUMAT gives energy dissipation due to composite damage. It can be seen that the titanium plies deform plastically until the impactor reverses. However, the slope of plastic dissipation changes at around 3 ms where the first significant drop in the force–time response is observed. This phenomena will be addressed later. The contribution of dissipated energy due to damage in composites and in interfaces is only 0.25% of the total energy. Most energy is absorbed by the thick titanium sheets surrounding the composite laminate. Energy dissipation due to damage is further analysed in Figure 8(c).

It is found that debonding between titanium and composite, and matrix failure within the composite, are the main drivers for dissipated energy related to damage. Debonding initiates slightly earlier and it dissipates more energy compared to matrix cracking.

In Figure 9(a), all failure modes implemented in Hashin's criteria are compared at a high energy level of 40 J. More than 80% of elements fail due to matrix cracks under tension. Only a small number of elements fail due to tensile fibre or compressive matrix failure after adjacent elements failed. No fibre failure in compression occurs. Figure 9(b) shows individual terms in Hashin's matrix failure criterion (10) in tension. It can be seen that the term including σ_{22} is the most
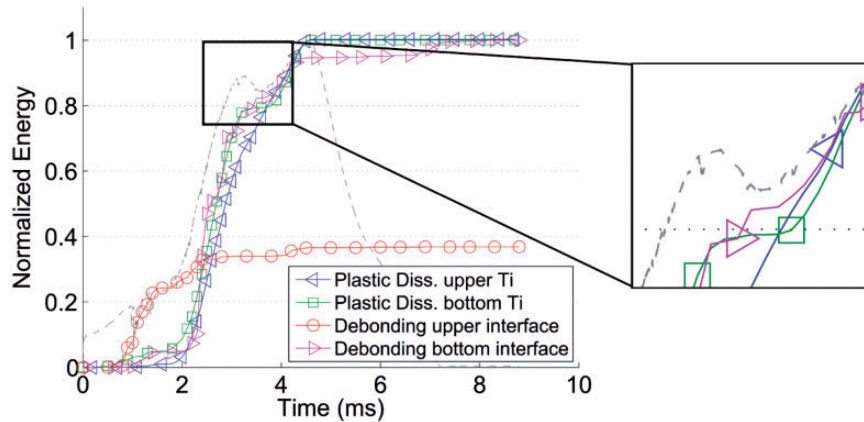
Figure 10: Analysis of first drop in impact response.

dominant which underlines again the idea that all failure criteria can be reduced to the classical maximum stress criterion. Terms including transverse stress evaluation only have a small contribution to Hashin's matrix failure criterion in this particular load case.

In order to explain the first significant drop in the force response for any energy level, Figure 10 shows the plastic dissipation due to impact in the upper and lower titanium sheet, respectively. Energy dissipated by debonding in the upper and lower titanium–composite interfaces is also shown. Ply failure investigated in Figure 9(a) is negligible, based on the energy analysis in Figure 8(b) and (c). To be able to relate the two failure mechanisms, plastic dissipation is normalised by maximum absorbed energy due to plasticity, whereas debonding energy is normalised by maximum dissipated energy due to debonding. Figure 8(b) and (c) show that they vary significantly in magnitude. It can be observed that the upper sheet dissipates energy at a constant rate up to the maximum force at around 5 ms. However, the bottom titanium sheet is not deforming plastically for a short time period at around 3 ms. This means that there is less force applied to that sheet. Afterwards, the sheet deforms plastically in the same way as the upper layer. A detailed view of the force response at the first drop in Figure 10 presents a possible explanation for this phenomenon. It shows that debonding in the bottom interface is not a continuous process. Furthermore, debonding starts early, as seen in Figure 8(c). Stress is concentrated in the interface until it partly debonds. At the time of the first drop, neither debonding nor plastic deformation occurs. This means that there is less resistance on the impactor for a short period of time. This can be explained by taking into account the optical damage inspection in Figure 4. The debonded area increases and creates a gap owing to the central part of the lower titanium bending significantly more than the composite laminate and the upper titanium. Thus, there is a decrease in force on
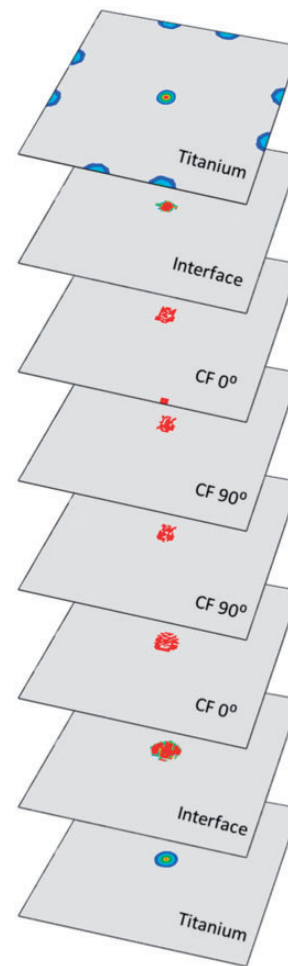

Figure 11: Damage model: plastic dissipation in titanium, matrix cracks in composite (CF) plies and debonding in interface.

the impactor until the upper part, consisting of titanium and composite laminate, closes the gap created by debonding.

Figure 11 illustrates individual layers of the model. It shows areas of plastic deformation in titanium layers,

debonding in cohesive interface elements and matrix failure in composite plies. These areas are mainly concentrated around the impact. Some plastic dissipation owing to clamping can be observed in the upper titanium layer. More damage is observed in the lower plies owing to bending. The damage area in the lower titanium ply and the lower interface layer is significantly larger than in the corresponding upper layer. This is also experimentally observed in the visual inspection in Figure 4.

Conclusion

Drop-weight LVI tests were conducted on HTCLs. Energy levels from 10 up to 40 J were investigated. The impact response shows a bilinear increase and one significant drop before the impactor reverses. Optical inspection shows that debonding in the titanium–composite interface and matrix cracking in tension are the major failure modes.

The numerical model addresses the lack of computational LVI tests on HTCL at high energy levels up to 40 J. Unlike similar numerical tests for pure composite laminates, the lower computational cost makes it suitable to effectively predict the impact response on conventional computers with a runtime analysis of less than one day by only considering experimentally identified major failure modes. Debonding between titanium and composite laminates is modelled by cohesive interfaces and titanium sheets by plastically deforming elements. The model is able to capture the major failure modes and the overall force response with reasonable accuracy. It is possible to relate experimentally observed and simulated damage evolution with physical mechanisms. It is found, and numerically quantified, that most of the energy is absorbed by the 0.5 mm thick titanium sheets on the outside. Numerical investigations in this paper show that under biaxial loading in thin plates with energy-absorbing sheets, such as the tested HTCL samples, various simplifications can be made to reduce complexity and computational cost. Different established failure theories in composite laminates are implemented in a user-written material subroutine in Abaqus. These complex failure criteria can be reduced to a simple maximum stress criterion. Furthermore, advanced damage evolution models can be simplified to instant damage initiation without the loss of accuracy. It should be noted that these findings are particular to HTCL systems and cannot be generalised to other FML systems with different interfacial or mechanical properties for which the structural response could not be simplified to such an extent.

Simulating high energy levels at 30 or 40 J, the numerical model overestimates the maximum force by approximately 20%. A finer mesh and an experimentally obtained characterisation of the titanium–composite interface will capture debonding more accurately. Zero-thickness cohesive elements between composite plies can further improve the prediction by taking interlaminar delamination into account. Moreover, boundary conditions could be modelled as independent instances[16] instead of simply restraining nodes. Most of the recommendations will, however, significantly increase runtime analysis and require clustering without particularly improving the overall accuracy.

Declaration of Conflicting Interests

The author(s) declared no potential conflicts of interest with respect to the research, authorship, and/or publication of this article.

Funding

References

1. Manikandan P and Chai G. A layer-wise behavioral study of metal based interply hybrid composites under low velocity impact load. *Composite Structures* 2014; 117(1): 17–31.

2. Caprino G, Spataro G and Del Luongo S. Low-velocity impact behaviour of fibreglass-aluminium laminates. *Composites A* 2004; 35(5): 605–616.

3. Wu G and Yang JM. The mechanical behavior of glare laminates for aircraft structures. *JOM* 2005; 57(1): 72–79.

4. Walz M. The dream of composites. *R&D Magazine*, 20 November 2006. Available at: http://www.rdmag.com/articles/2006/11/dream-composites [accessed 17 December 2006].

5. Burianek D and Spearing S. Fatigue damage in titanium-graphite hybrid laminates. *Composites Sci Technol* 2002; 62(5): 607–617.

6. Blackwood D, Chua A, Seah K, et al. Corrosion behaviour of porous titanium-graphite composites designed for surgical implants. *Corrosion Sci* 2000; 42(3): 481–503.

7. Kim D and Ramulu M. Study on the drilling of titanium/graphite hybrid composites. *J Eng Mater Technol* 129(3): 390–396.

8. Boyer R. Attributes, characteristics, and applications of titanium and its alloys. *JOM* 2010; 62(5): 21–24.

9. Papakonstantinou C and Katakalos K. Mechanical behavior of high temperature hybrid carbon fiber/titanium laminates. *J Eng Mater Technol, Trans ASME* 2009; 131(2): 021008.

10. Liu Y and Liaw B. Effects of constituents and lay-up configuration on drop-weight tests of fiber-metal laminates. *Appl Compos Mater* 2010; 17(1): 43–62.

11. Alderliesten R, Hagenbeek M, Homan J, et al. Fatigue and damage tolerance of glare. *Appl Compos Mater* 2003; 10(4–5): 223–242.

12. Wu G, Yang JM and Hahn H. The impact properties and damage tolerance and of bi-directionally reinforced fiber metal laminates. *J Mater Sci* 2007; 42(3): 948–957.

13. Bernhardt S, Ramulu M and Kobayashi A. Low-velocity impact response characterization of a hybrid titanium composite laminate. *J Eng Mater Technol, Trans ASME* 2007; 129(2): 220–226.

14. Cortes P and Cantwell W. The tensile and fatigue properties of carbon fiber-reinforced peek-titanium fiber-metal laminates. *J Reinf Plastics Composites* 2004; 23(15): 1615–1623.

15. González E, Maimí P, Camanho P, et al. Simulation of drop-weight impact and compression after impact tests on composite laminates. *Composite Structures* 2012; 94(11): 3364–3378.

16. Perillo G, Vedivik N and Echtermeyer A. Damage development in stitch bonded gfrp composite plates under low velocity impact: Experimental and numerical results. *J Composite Mater* 2015; 49(5): 601–615.

17. Camanho P, Dávila C and De Moura M. Numerical simulation of mixed-mode progressive delamination in composite materials. *J Composite Mater* 2003; 37(16): 1415–1438.

18. Puck A and Schürmann H. Failure analysis of {FRP} laminates by means of physically based phenomenological models. *Composites Sci Technol* 2002; 62(12–13): 1633–1662.

19. Hashin Z and Rotem A. Fatigue failure criterion for fiber reinforced materials. *J Composite Mater* 1973; 7: 448–464.

20. Nakatani H, Kosaka T, Osaka K, et al. Facesheet effects on the low velocity impact damages in titanium/GFRP hybrid laminates. *ICCM international conferences on composite materials*. .

21. Peters WH and Ranson WF. Digital imaging techniques in experimental stress analysis. *Opt Eng* 1982; 21(3): 213427.

22. Fink A, Camanho P, Andrés J, et al. Hybrid CFRP/titanium bolted joints: Performance assessment and application to a spacecraft payload adaptor. *Composites Sci Technol* 2010; 70(2): 305–317.

23. Kennedy A, Kohler R and Poole P. A sodium hydroxide anodize surface pretreatment for the adhesive bonding of titanium alloys. *Int J Adhesion Adhesives* 1983; 3(3): 133–139.

24. Maimí P, Camanho P, Mayugo J, et al. A continuum damage model for composite laminates: Part I – constitutive model. *Mech Mater* 2007; 39(10): 897–908.

25. Matzenmiller A, Lubliner J and Taylor R. A constitutive model for anisotropic damage in fiber-composites. *Mech Mater* 1995; 20(2): 125–152.

26. Maimí P, Camanho P, Mayugo J, et al. A continuum damage model for composite laminates: Part II – computational implementation and validation. *Mech Mater* 2007; 39(10): 909–919.

27. Bažant Z, Kim J, Daniel I, et al. Size effect on compression strength of fiber composites failing by kink band propagation. *Int J Fracture* 1999; 95(1–4): 103–141.

28. Tsai SW and Wu EM. General theory of strength for anisotropic materials. *J Composite Mater* 1971; 5: 58–80.

29. Turon A, Camanho P, Costa J, et al. A damage model for the simulation of delamination in advanced composites under variable-mode loading. *Mech Mater* 2006; 38(11): 1072–1089.

30. *Abaqus Version 6.11 User's manual*. Dassault Systemes Simulia Corp, 2011.

31. Turon A, Dávila C, Camanho P, et al. An engineering solution for mesh size effects in the simulation of delamination using cohesive zone models. *Eng Fracture Mech* 2007; 74(10): 1665–1682.

32. R Wisnom M and Chang FK. Modelling of splitting and delamination in notched cross-ply laminates. *Composites Sci Technol* 2000; 60(15): 2849–2856.

33. Benzeggagh M and Kenane M. Measurement of mixed-mode delamination fracture toughness of unidirectional glass/epoxy composites with mixed-mode bending apparatus. *Composites Sci Technol* 1996; 56(4): 439–449.

34. Jones RM. *Mechanics of composite materials*, 2nd ed. Philadelphia, PA: Taylor & Francis, 1999.

35. Narayanaswami R and Adelman HM. Evaluation of the tensor polynomial and Hoffman strength theories for composite materials. *J Composite Mater* 1977; 11(4): 366–377.

36. Hexcel Corporation. *HexPly M18/1 Datasheet*, 2007.

37. Lagunegrand L, Lorriot T, Harry R, et al. Initiation of free-edge delamination in composite laminates. *Composites Sci Technol* 2006; 66(10): 1315–1327.

38. Sebaey T, Costa J, Maimí P, et al. Measurement of the in situ transverse tensile strength of composite plies by means of the real time monitoring of microcracking. *Composites B* 2014; 65: 40–46.

Appendix: Failure criteria

In the following, subscripts 11, 22 and 33 indicate strain, stress or strength in fibre and transverse direction, whereas 12, 23 and 13 indicate shear. Furthermore, X and Y represent fibre and matrix strength in a composite in tension T and compression C, respectively.

Hashin.[19]

1. Tensile fibre failure for $\sigma_{11} > 0$

$$\phi_{H1+} = \left(\frac{\sigma_{11}}{X_T}\right)^2 + \frac{\sigma_{12}^2 + \sigma_{13}^2}{S_{12}^2} \qquad (8)$$

2. Compressive fibre failure for $\sigma_{11} < 0$

$$\phi_{H1-} = \left(\frac{\sigma_{11}}{X_C}\right)^2 \qquad (9)$$

3. Tensile matrix failure for $\sigma_{22} + \sigma_{33} > 0$

$$\phi_{\mathrm{H2+}} = \frac{(\sigma_{22} + \sigma_{33})^2}{Y_T^2} + \frac{\sigma_{23}^2 - \sigma_{22}\sigma_{33}}{S_{23}^2} + \frac{\sigma_{12}^2 + \sigma_{13}^2}{S_{12}^2} \quad (10)$$

4. Compressive matrix failure for $\sigma_{22} + \sigma_{33} < 0$

$$\phi_{\mathrm{H2-}} = \left[\left(\frac{Y_C}{2S_{23}}\right)^2 - 1 \right] \left(\frac{\sigma_{22} + \sigma_{33}}{Y_C}\right)$$
$$+ \frac{(\sigma_{22} + \sigma_{33})^2}{4S_{23}^2} + \frac{\sigma_{23}^2 - \sigma_{22}\sigma_{33}}{S_{23}^2} + \frac{\sigma_{12}^2 + \sigma_{13}^2}{S_{12}^2}$$
$$(11)$$

Puck.[18]

1. Tensile fibre failure for $\epsilon_1 > 0$ (classical maximum strain criterion)

$$\phi_{\mathrm{P1+}} = \frac{\epsilon_{11}}{\epsilon_T} \quad (12)$$

2. Compressive fibre failure for $\epsilon_1 < 0$

$$\phi_{\mathrm{P1-}} = \frac{\epsilon_{11}}{\epsilon_C} \quad (13)$$

3. Tensile matrix failure for $\sigma_{22} > 0$ (simplified version)

$$\phi_{\mathrm{P2+}} = \frac{p_{\perp\psi}^+}{S_{23}} \sigma_{22}$$
$$+ \sqrt{ \left[\left(\frac{1}{Y_T} - \frac{p_{\perp\psi}^+}{S_{23}}\right)\sigma_{22} \right]^2 + \left(\frac{\sigma_{12}}{S_{12}}\right)^2 + \left(\frac{\sigma_{23}}{Y_{C1}}\right)^2 }$$
$$(14)$$

4. Compressive matrix failure for $\sigma_{22} < 0$

$$\phi_{\mathrm{P2-}} = \frac{p_{\perp\psi}^-}{S_{23}} \sigma_{22}$$
$$+ \sqrt{ \left(\frac{\sigma_{12}}{S_{12}}\right)^2 + \left(\frac{\sigma_{23}}{Y_{C1}}\right)^2 + \left[\left(\frac{p_{\perp\psi}^-}{S_{23}}\right)\sigma_{22} \right]^2 }$$
$$(15)$$

with parameters (Table 3)

$$Y_{C1} = \frac{Y_C}{2(1 + p_{\perp\perp}^-)} \quad (16)$$

Table 3: Puck parameters.[18]

	$p_{\perp\parallel}^+$	$p_{\perp\parallel}^-$	$p_{\perp\perp}^+$	$p_{\perp\perp}^-$
Glass fibre	0.30	0.25	0.2–0.25	0.2–0.25
Carbon fibre	0.35	0.30	0.25–0.30	0.25–0.30

and

$$p_{\perp\psi}^+ = S_{23}\left(\frac{p_{\perp\perp}^+}{Y_{C1}}(\cos\psi)^2 + \frac{p_{\perp\parallel}^+}{S_{12}}(\sin\psi)^2 \right)$$
$$p_{\perp\psi}^- = S_{23}\left(\frac{p_{\perp\perp}^-}{Y_{C1}}(\cos\psi)^2 + \frac{p_{\perp\parallel}^-}{S_{12}}(\sin\psi)^2 \right)$$
$$(17)$$

where ψ is given by

$$(\cos\psi)^2 = \frac{\sigma_{23}^2}{\sigma_{23}^2 + \sigma_{12}^2}$$
$$(\sin\psi)^2 = \frac{\sigma_{12}^2}{\sigma_{23}^2 + \sigma_{12}^2}$$
$$(18)$$

Tsai–Wu. Under plane stress assumptions, the Tsai–Wu failure criterion is given by[34]

$$\phi_{\mathrm{TW}} = F_1\sigma_1 + F_2\sigma_2 + F_6\sigma_6 + F_{11}\sigma_1^2 + F_{22}\sigma_2^2$$
$$+ F_{66}\sigma_6^2 + 2F_{12}\sigma_1\sigma_2$$
$$(19)$$

with components

$$F_1 = \frac{1}{X_T} + \frac{1}{X_C}, \qquad F_{11} = -\frac{1}{X_T X_C} \quad (20)$$

$$F_2 = \frac{1}{Y_T} + \frac{1}{Y_C}, \qquad F_{22} = -\frac{1}{Y_T Y_C} \quad (21)$$

and

$$F_{66} = \frac{1}{S_{12}^2} \quad (22)$$

As outlined by Jones,[34] $F_6 = 0$. Moreover, F_{12} can be neglected.[35]